INTERNATIONAL JOURNAL FOR NUMERICAL AND ANALYTICAL METHODS IN GEOMECHANICS

Numerical Simulation of Fully Saturated Porous Materials

Boris Jeremić (Борис Јеремић)[1,*]

Zhao Cheng (程 昭)[2]

Mahdi Taiebat (مهدی طیبات)[3]

and Yannis Dafalias (Ιωάννης Δαφαλιάς)[4]

[1] *Associate Professor, Department of Civil and Environmental Engineering, University of California, Davis, CA 95616.* `jeremic@ucdavis.edu`

[2] *Staff Engineer, Earth Mechanics Inc. Oakland, CA 94621*

[3] *Graduate Student, Department of Civil and Environmental Engineering, University of California, Davis, CA 95616.*

[4] *Professor, Department of Civil and Environmental Engineering, University of California, Davis, CA 95616 and Department of Mechanics, National Technical University of Athens, Zographou 15780, Greece.*

[*]Correspondence to: Boris Jeremić, Department of Civil and Environmental Engineering, University of California, One Shields Ave., Davis, CA 95616, `jeremic@ucdavis.edu`

Contract/grant sponsor: NSF; contract/grant number: EEC-9701568

Contract/grant sponsor: NSF; contract/grant number: CMS–0337811

Abstract Fully coupled, porous solid-fluid formulation, implementation and related modeling and simulation issues are presented in this work. To this end, coupled dynamic field equations with $u-p-U$ formulation are used to simulate pore fluid and soil skeleton (elastic–plastic porous solid) responses. Present formulation allows, among other features, for water accelerations to be taken into account. This proves useful in modeling dynamic interaction of media of different stiffness (as in soil–foundation–structure interaction). Fluid compressibility is also explicitly taken into account, thus allowing excursions into modeling of limited cases of non-saturated porous media. In addition to those feature, present formulation and implementation models in a realistic way the physical damping, which dissipates energy. In particular, the velocity proportional damping is appropriately modeled and simulated by taking into account interaction of pore fluid and solid skeleton. Similarly, the displacement proportional damping is physically modeled trough elastic–plastic processes in soil skeleton. An advanced material model for sand is used in presented work and is discussed at some length. Also explored in this paper are verification and validation issues related to fully coupled modeling and simulations of porous media.

Illustrative examples describing dynamical behavior of porous media (saturated soils) are presented. The verified and validated methods and material models are used to *predict* behavior of level and sloping grounds subjected to seismic shaking.

KEY WORDS: Elasto–plastic, Finite elements, Saturated porous solid–fluid simulations, Soil dynamics

1. Introduction

Modeling and simulations of soil behavior induced by earthquakes, that can be related to liquefaction and cyclic mobility, continue to challenge engineering research and practice. Such behavior commonly occurs in loose to medium dense sands which are fully saturated and will results the almost complete loss of strength (liquefaction), and partial loss of strength (cyclic mobility). To model these complex phenomena, a consistent and efficient coupled formulation must be utilized, including an accurate single-phase constitutive model for soil. Three general continuum formulations (Zienkiewicz and Shiomi, 1984) are possible for modeling of the fully coupled problem (soil skeleton – pore fluid) in geomechanics, namely the (a) $u-p$, (b) $u-U$, and (c) $u-p-U$ formulations. Here, the unknowns are the soil skeleton displacements u; the pore fluid (water) pressure p; and the pore fluid (water) displacements U. The $u-p$ formulation captures the movements of the soil skeleton and the change of the pore pressure, and is the most simplistic one of the three mentioned above. This formulation neglects the accelerations of the pore fluid (except for combined (same) acceleration of pore fluid and solid), and in one version neglects the compressibility of the fluid (assuming complete incompressibility of the pore fluid). In the case of incompressible pore fluid and very low permeability, the formulation requires special treatment of the approximation (shape) function for pore fluid to prevent the volumetric locking (Zienkiewicz and Taylor, 2000). This formulation also must rely on Rayleigh damping to model velocity proportional energy dissipation (damping). The majority of the currently available implementations are based on this formulation. For example Elgamal et al. (2002) and Elgamal et al. (2003) developed an implementation of the $u-p$ formulation with the multi-surface plasticity model of Prevost (1985), while Chan (1988) and Zienkiewicz et al. (1999) used generalized theory of plasticity by Pastor et al. (1990) in their simulations.

In addition to that Taiebat et al. (2007) used the constitutive model by Manzari and Dafalias (1997) in their $u-p$ formulation and showed good model performance for capturing the response in a boundary value problem from VELACS project Arulanandan and Scott (1993). We also note earlier works by Zienkiewicz et al. (1980), Simon et al. (1984b,a), S.Sandhu et al. (1990) and Gajo et al. (1994).

The $u-U$ formulations tracks the movements of both the soil skeleton and the pore fluid. This formulation is complete in the sense of basic variable, but might still experience numerical problems (volumetric locking) if the difference in volumetric compressibility of the pore fluid and the solid skeleton is large.

The $u-p-U$ formulation resolves the issues of volumetric locking by including the displacements of both the solid skeleton and the pore fluid, and the pore fluid pressure as well. This formulation uses additional (dependent) unknown field of pore fluid pressures to stabilize the solution of the coupled system. The pore fluid pressures are connected to (dependent on) displacements of pore fluid, as, with known volumetric compressibility of the pore fluid, pressure can be calculated. All three formulations were originally derived by Zienkiewicz and Shiomi (1984) and are critically discussed in Zienkiewicz et al. (1999).

Despite it's power, the $u-p-U$ formulation has rarely been implemented into finite element code. In this paper, complete $u-p-U$ formulation and implementation is presented. A set of verification examples are used to determine that formulation and the implementation accurately represent conceptual description of porous media behavior[†]. In addition to that, a recent critical state two-surface plasticity model accounting for the fabric dilation effects

[†]Verification is a mathematics issue. It provides evidence that the model is solved correctly.

(Dafalias and Manzari, 2004) is described in some details as well. The material model behavior is validated using a number of constitutive tests from literature. The validation process is important in determining the degree to which a model is accurate representation of the real world from the perspective of the intended uses of the model[‡]. Issues of verification and validation are fundamental to the process of prediction of mechanical behavior in computational science and engineering (Oberkampf et al., 2002; Roache, 1998).

A number of predictive examples are presented in a later part of the paper. The examples rely on verified formulation and implementation of behavior of fully coupled porous media and on validated constitutive material modeling. Predictive examples consist of level and sloping grounds excited by seismic shaking at the base. Examples explore behavior (displacements of solid skeleton and pore fluid, excess pore pressure, stress-strain) for two different types (dense and loose) of Toyoura sand.

2. Formulation, Finite Element Discretization and Implementation

This section briefly reviews equations describing behavior of solid skeleton and pore fluid and their interaction. It is important to note the sign convention used in developments described in this paper. The compression stress is assumed negative here (as is common in mechanics of materials), and the effect of this sign convention has been considered on the model equations. For example this is the reason for having couple of different signs in the equations comparing to the original work by Dafalias and Manzari (2004). The mean effective stress p is defined as $p = -\sigma'_{ii}/3$ and therefore is positive in compression. The deviatoric stress tensor s_{ij} then

[‡]Validation is a physics issue. It provides evidence that the correct model is solved.

can be obtained using $s_{ij} = \sigma^{'}_{ij} + p\delta_{ij}$. As for the (small) strain tensor $\epsilon_{ij} = (u_{i,j} + u_{j,i})/2$, the volumetric component is defined as $\epsilon_v = \epsilon_{ii}$, while the deviatoric strain tensor e_{ij} can be obtained from $e_{ij} = \epsilon_{ij} - \epsilon_v \delta_{ij}/3$.

2.1. Governing Equations of Porous Media

The material behavior of soil skeleton is fully dependent on the pore fluid pressures. The behavior of pore fluid is assumed to be elastic and thus all the material nonlinearity is concentrated in the soil skeleton. The soil behavior (mix of soil skeleton and pore fluid) can thus be described using single–phase constitutive analysis approach for skeleton combined with the full coupling with pore fluid. The concept of effective stress of the saturated mixture, that is, the relationship between effective stress, total stress and pore pressure (Zienkiewicz et al., 1999) can be written as $\sigma^{'}_{ij} = \sigma_{ij} + \alpha\delta_{ij}p$, where $\sigma^{'}_{ij}$ is the effective stress tensor, σ_{ij} is total stress tensor, δ_{ij} is Kronecker delta and α is the Biot constant that depends on the geometry of material voids. For the most part, in soil mechanics problems, $\alpha \approx 1$ can be assumed. The relation between total and effective stress becomes $\sigma^{'}_{ij} = \sigma_{ij} + \delta_{ij}p$, which corresponds to the classical effective stress definition by Terzaghi (1943).

The overall equilibrium or momentum balance equation for the soil-fluid 'mixture' can be written as

$$\sigma_{ij,j} - \rho\ddot{u}_i - \rho_f \ddot{w}_i + \rho b_i = 0 \tag{1}$$

where $\ddot{u}_i$ is the acceleration of the solid part, b_i is the body force per unit mass, $\ddot{w}_i$ is the fluid acceleration relative to the solid part. For fully saturated porous media (no air trapped inside), density is equal to $\rho = n\rho_f + (1-n)\rho_s$, where n is the porosity, ρ_s and ρ_f are the soil particle and water density respectively.

For the pore fluid, the equation of momentum balance can be written as

$$-p_{,i} - R_i - \rho_f \ddot{w}_i - \frac{\rho_f \ddot{w}_i}{n} + \rho_f b_i = 0 \tag{2}$$

where R is the viscous drag force. According to the Darcy's seepage law, the viscous drag forces R between soil matrix and pore fluid (water) can be written as $R_i = k_{ij}^{-1} \dot{w}_j$, where k_{ij} is the tensor of anisotropic Darcy permeability coefficients. For simple case of isotropic permeability, scalar value of permeability k is used. The permeability k used here with dimension of $[L^3 T M^{-1}]$ is different from the permeability used in the usual soil mechanics (K) which has the same dimension of velocity, i.e. $[LT^{-1}]$. Their values are related by $k = K/g\rho_f$, where g is the gravitational acceleration and the permeability K is measured in an experiment.

The final equation is the mass conservation of the fluid flow expressed by

$$\dot{w}_{i,i} + \alpha \dot{\varepsilon}_{ii} + \frac{\dot{p}}{Q} = 0 \tag{3}$$

where bulk stiffness of the mixture Q is expressed as $1/Q = n/K_f + (\alpha - n)/K_s$ and K_s and K_f are the bulk moduli of the solid and fluid phases respectively.

In the above governing equations, convective and terms of lower order are omitted (Zienkiewicz et al., 1999). A change of variable is performed by introducing an alternative variable U_i, defined as $U_i = u_i + U_i^R = u_i + w_i/n$, that represents absolute displacement of the pore fluid. The basic set of unknowns is then comprised of the soil skeleton displacements u_i, the water pore pressure p, and the water displacements U_i.

2.2. Finite Element Formulation

Standard finite element discretization (Zienkiewicz and Taylor, 1991a,b) uses shape functions to describe each of the unknown fields (u–p–U) in terms of nodal values (solid displacements

$\bar{u}_{Ki}$, pore fluid pressures $\bar{p}_K$, and pore fluid displacements $\bar{U}_{Ki}$):

$$u_i = N_K^u \bar{u}_{Ki}, \quad p = N_K^p \bar{p}_K, \quad U_i = N_K^U \bar{U}_{Ki} \tag{4}$$

where N_K^u, N_K^p and N_K^U are (same) shape functions for solid displacement, pore pressure and fluid displacement respectively. Each node of the (u–p–U) element has thus seven degrees of freedoms in 3 dimensions (three for solid displacements, one for pore fluid pressures and three or pore fluid displacements). It should be noted that it is possible to use same shape functions for both displacement and pore pressure unknown field as u–p–U formulation with compressible fluid allows that without volumetric locking (Zienkiewicz and Shiomi, 1984).

By using finite element discretization and after some tensor algebra and manipulations, the weak form of governing equations can be obtained from the strong form described by Equations (1), (2) and (3). The weak form is presented in tensor notation (see Zienkiewicz and Taylor (1991a) chapter 6.) as

$$\begin{bmatrix} (M_s)_{KijL} & 0 & 0 \\ 0 & 0 & 0 \\ 0 & 0 & (M_f)_{KijL} \end{bmatrix} \begin{bmatrix} \ddot{\bar{u}}_{Lj} \\ \ddot{\bar{p}}_N \\ \ddot{\bar{U}}_{Lj} \end{bmatrix} + \begin{bmatrix} (C_1)_{KijL} & 0 & -(C_2)_{KijL} \\ 0 & 0 & 0 \\ -(C_2)_{LjiK} & 0 & (C_3)_{KijL} \end{bmatrix} \begin{bmatrix} \dot{\bar{u}}_{Lj} \\ \dot{\bar{p}}_N \\ \dot{\bar{U}}_{Lj} \end{bmatrix}$$
$$+ \begin{bmatrix} 0 & -(G_1)_{KiM} & 0 \\ -(G_1)_{LjM} & -P_{MN} & -(G_2)_{LjM} \\ 0 & -(G_2)_{KiL} & 0 \end{bmatrix} \begin{bmatrix} \bar{u}_{Lj} \\ \bar{p}_M \\ \bar{U}_{Lj} \end{bmatrix}$$
$$+ \begin{bmatrix} \int_\Omega N_{K,j}^u \sigma_{ij}^{'} \mathrm{d}\Omega \\ 0 \\ 0 \end{bmatrix} - \begin{bmatrix} \bar{f}_{Ki}^u \\ 0 \\ \bar{f}_{Ki}^U \end{bmatrix} = 0 \tag{5}$$

The left hand side components of the above matrix equation are given as:

$$
\begin{aligned}
(M_s)_{KijL} &= \int_\Omega N_K^u (1-n)\rho_s \delta_{ij} N_L^u \mathrm{d}\Omega \quad ; \quad (M_f)_{KijL} = \int_\Omega N_K^U n \rho_f \delta_{ij} N_L^U \mathrm{d}\Omega \\
(C_1)_{KijL} &= \int_\Omega N_K^u n^2 k_{ij}^{-1} N_L^u \mathrm{d}\Omega \quad ; \quad (C_2)_{KijL} = \int_\Omega N_K^u n^2 k_{ij}^{-1} N_L^U \mathrm{d}\Omega \\
(C_3)_{KijL} &= \int_\Omega N_K^U n^2 k_{ij}^{-1} N_L^U \mathrm{d}\Omega \quad ; \quad (G_1)_{KiM} = \int_\Omega N_{K,i}^u (\alpha - n) N_M^p \mathrm{d}\Omega \\
(G_2)_{KiM} &= \int_\Omega n N_{K,i}^U N_M^p \mathrm{d}\Omega \quad ; \quad P_{NM} = \int_\Omega N_N^p \frac{1}{Q} N_M^p \mathrm{d}\Omega
\end{aligned} \tag{6}
$$

while the right hand side components are given as:

$$
\begin{aligned}
(\bar{f}_s)_{Ki} &= \int_{\Gamma_t} N_K^u \sigma_{ij}^{'} n_j \mathrm{d}\Gamma - \int_{\Gamma_p} N_K^u (\alpha - n) p n_i \mathrm{d}\Gamma + \int_\Omega N_K^u (1-n) \rho_s b_i \mathrm{d}\Omega \\
(\bar{f}_f)_{Ki} &= -\int_{\Gamma_p} N_K^U n p n_i \mathrm{d}\Gamma + \int_\Omega N_K^U n \rho_f b_i \mathrm{d}\Omega
\end{aligned} \tag{7}
$$

It is very important to note that the velocity proportional damping was introduced directly through the damping tensor (or matrix) with components $(C_1)_{KijL}$, $(C_2)_{KijL}$ and $(C_3)_{KijL}$, which are functions of porosity and permeability of the skeleton. This damping provides for physically based energy dissipation due to interaction of pore fluid and the solid (soil) skeleton. It is also emphasized again that presented formulation and implementation do not use Rayleigh damping.

2.3. Constitutive Integration

In work presented, an explicit version of constitutive driver was used for Dafalias–Manzari model. While the implicit constitutive integrations (Jeremić and Sture, 1997) are preferred for local interactions, some material models have a highly nonlinear regions in the yield surface, plastic flow directions and/or evolution laws. The Dafalias–Manzari material model (Dafalias and Manzari, 2004) used in this study, exhibits such behavior, particularly in the very low mean effective stress region, which is of much interest here. Implicit constitutive integration in such regions are highly unstable as the stress and internal variable state is far from the so called trust region of the underlying Newton method (see more in Dennis and Schnabel (1983)). One possible solution for every failed implicit step is to try the line search algorithm (Jeremić (2001)). However, while line search (eventually) automatically achieves solution, it also tends to create very short steps. This stems from the fact that line search keeps cutting in half Newton steps that fail to converge. In addition to that, implicit integrations feature much higher computational load per step compared to explicit integrations, leading to slower computations. Eventual benefit of implicit integration in faster global Newton solution, was not pursued in this work but will be investigated in future publications. All of the above reasons led us to use explicit integration algorithm in this work.

The Explicit (forward Euler) method is based on starting point of plastic flow in the stress and internal variable space for finding all the relevant derivatives. The increment of stress and internal variables is given by

$$\Delta\sigma^{'}_{mn} = {}^{c}E_{mnpq}\,\Delta\epsilon^{ep}_{pq} - {}^{c}E_{mnpq}\,\frac{{}^{c}n_{rs}\;{}^{c}E_{rstu}\;\Delta\epsilon^{ep}_{tu}}{{}^{c}n_{ab}\;{}^{c}E_{abcd}\;{}^{c}m_{cd} - {}^{n}\xi_{A}{}^{n}h_{A}}\;{}^{c}m_{pq} \tag{8}$$

$$\Delta q_{A} = \left(\frac{{}^{c}n_{mn}\;{}^{c}E_{mnpq}\;\Delta\epsilon^{ep}_{pq}}{{}^{c}n_{mn}\;{}^{c}E_{mnpq}\;{}^{c}m_{pq} - {}^{n}\xi_{A}{}^{n}h_{A}}\right)h_{A} \tag{9}$$

It is important to note that the explicit algorithm performs only one step of the computation and does not check on the convergence of the provided solutions. This usually results in the slow drift of the stress–internal variable point from the yield surface for monotonic loading. The use of Explicit integration can also result in spurious elastic–plastic deformations during elastic unloading in cyclic loading-unloading (Jeremić and Yang, 2002). In addition to that, the Explicit integrations can lead to completely erroneous step if the load reversal step is large enough that the stress path misses the elastic region and lands in elastic–plastic region on the opposite side of yield surface. In this case, derivatives of yield surface, plastic flow directions and derivatives of evolution law from the starting point will point one way, while the actual starting point should be on the other side of the yield surface. Both spurious elastic–plastic step and inconsistency in starting point need to be carefully watched for during computations.

2.4. Time Integration

In order to develop integration of dynamic finite element equation in the time domain, Equation (5) is rewritten in a residual matrix form (Argyris and Mlejnek, 1991)

$$\mathbf{R} = \mathbf{M}\ddot{\mathbf{x}} + \mathbf{C}\dot{\mathbf{x}} + \mathbf{K}'\mathbf{x} + \mathbf{F}(\mathbf{x}) - \mathbf{f} = \mathbf{0} \tag{10}$$

where $\mathbf{x} = \{\bar{\mathbf{u}}, \bar{\mathbf{p}}, \bar{\mathbf{U}}\}^{\mathbf{T}}$ represent a vector of generalized unknown variables. Equation (10) represents the general non-linear form (Argyris and Mlejnek, 1991) for which the usual tangent stiffness $\mathbf{K}$ does not equal to $\mathbf{K}'$, but instead,

$$\mathbf{K} = \frac{\partial \mathbf{R}}{\partial \mathbf{x}} = \mathbf{K}' + \frac{\partial \mathbf{F}(\mathbf{x})}{\partial \mathbf{x}} \tag{11}$$

In the specific case of $u-p-U$ formulation of interest here one can write matrix form

$$\mathbf{M} = \begin{bmatrix} \mathbf{M_s} & 0 & 0 \\ 0 & 0 & 0 \\ 0 & 0 & \mathbf{M_f} \end{bmatrix}, \quad \mathbf{C} = \begin{bmatrix} \mathbf{C_1} & 0 & -\mathbf{C_2} \\ 0 & 0 & 0 \\ -\mathbf{C_2^T} & 0 & \mathbf{C_3} \end{bmatrix} \tag{12}$$

$$\mathbf{K}' = \begin{bmatrix} 0 & -\mathbf{G_1} & 0 \\ -\mathbf{G_1^T} & -\mathbf{P} & -\mathbf{G_2^T} \\ 0 & -\mathbf{G_2} & 0 \end{bmatrix}, \quad \mathbf{K} = \begin{bmatrix} \mathbf{K^{ep}} & -\mathbf{G_1} & 0 \\ -\mathbf{G_1^T} & -\mathbf{P} & -\mathbf{G_2^T} \\ 0 & -\mathbf{G_2} & 0 \end{bmatrix} \tag{13}$$

where

$$\mathbf{K^{ep}} = (K^{ep})_{KijL} = \int_\Omega N^u_{K,m} E^{ep}_{imjn} N^u_{L,n} \mathrm{d}\Omega \tag{14}$$

The above set of residual (nonlinear) dynamic equations is solved using, usually, one of the two procedure, namely the Newmark (Newmark, 1959) and the Hilber–Hughes–Taylor (HHT) α–method (Hilber et al., 1977; Hughes and Liu, 1978a,b).

Newmark Integrator. The Newmark time integration method (Newmark, 1959) has two parameters, β and γ, and is described by the following two equations:

$$ {}^{n+1}x = {}^{n}x + \Delta t \; {}^{n}\dot{x} + \Delta^2 t \; [(\frac{1}{2} - \beta) \; {}^{n}\ddot{x} + \beta \; {}^{n+1}\ddot{x}] \tag{15} $$

$$ {}^{n+1}\dot{x} = {}^{n}\dot{x} + \Delta t \; [(1-\gamma) \; {}^{n}\ddot{x} + \gamma \; {}^{n+1}\ddot{x}] \tag{16} $$

which give the relations between the time step n to the next time step $n+1$. The method is an implicit, except when both β and γ are zero.

If the parameters β and γ satisfy the following conditions

$$ \gamma \geq \frac{1}{2}, \quad \beta = \frac{1}{4}(\gamma + \frac{1}{2})^2 \tag{17} $$

the time integration method is unconditionally stable. Any γ value greater than 0.5 will introduce numerical damping. Well-known members of the Newmark time integration method family include: trapezoidal rule or average acceleration method for $\beta = 1/4$ and $\gamma = 1/2$, linear acceleration method for $\beta = 1/6$ and $\gamma = 1/2$, and (explicit) central difference method for $\beta = 0$ and $\gamma = 1/2$. If and only if $\gamma = 1/2$, the accuracy is second-order (Hughes, 1987).

Hilber–Hughes–Taylor Integrator. The HHT time integration method uses an alternative residual form by introducing an addition parameter α to improve the performance:

$$ {}^{n+1}R = M \; {}^{n+1}\ddot{x} + (1+\alpha) F({}^{n+1}\dot{x}, {}^{n+1}x) - \alpha F({}^{n}\dot{x}, {}^{n}x) - \; {}^{n+1}f \tag{18} $$

while retaining the rest of Newmark equations (15) and (16) and its parameters β and γ. If the parameters α, β and γ satisfy

$$-1/3 \leq \alpha \leq 0, \quad \gamma = \frac{1}{2}(1-2\alpha), \quad \beta = \frac{1}{4}(1-\alpha)^2 \tag{19}$$

the HHT method is unconditionally stable and second-order accurate (Hughes, 1987).

2.5. Program Implementation

Implementation of the described algorithms and procedures was performed using a number of numerical libraries. Parts of OpenSees framework (McKenna, 1997) were used to connect the finite element domain. In particular, Finite Element Model Classes from OpenSees (namely, class abstractions for Node, Element, Constraint, Load and Domain) where used to describe the finite element model and to store the results of the analysis performed on the model. In addition to these, Analysis Classes were used to drive the global level finite element analysis, i.e., to form and solve the global system of equations. As for the Geomechanics modules, a number of elements, algorithms and material models from UCD Computational Geomechanics toolset are used. In particular, set of NewTemplate3Dep numerical libraries were used for constitutive level integrations, nDarray numerical libraries (Jeremić and Sture, 1998) were used to handle vector, matrix and tensor manipulations, while FEMtools element libraries were used coupled finite elements (u-p-U) and for element level computations. Finally, solvers from the uMfPACK set of libraries (Davis and Duff, 1997) were used to solve the nonsymmetric global (finite element level) system of equations.

All of the above libraries are available either through their original developers or through first Author's web site `http://geomechanics.ucdavis.edu`.

3. Material Model

The constitutive model plays a very important role in numerical simulation of the soil response. Within the critical state soil mechanics framework, Manzari and Dafalias (1997) proposed a two-surface critical state plasticity model for sands. Employing the effects of the state parameter on the behavior of sand, this model presents well-established mechanisms for prediction of softening/hardening as well as dilatancy/contractancy response in different loose and dense states of sand. Dafalias and Manzari (2004) later presented an improved version of the model. This version introduced the fabric-dilatancy tensor which has a significant effect on the contraction unloading response. This version also considered the effect of a modified Lode angle on the flow rule, which produces more realistic responses in non-triaxial conditions. For the sake of completeness of the paper, the essential elements of this plasticity model are summarized and presented here with index notation.

3.1. Critical State Line

The constitutive model proposed by Dafalias and Manzari (2004) is essentially based on the critical state soil mechanics framework and the defining the correct position of the CSL is important in this model. Instead of using the common linear relation of the critical void ratio e_c v.s. the logarithm of the critical mean effective stress p_c, they have adopted a power relation, suggested by Li and Wang (1998), which gives a greater freedom in representing the Critical State Line:

$$e_c = e_{c,r} - \lambda_c \left(\frac{p_c}{p_{at}} \right)^{\xi} \tag{20}$$

where $e_{c,r}$ is the reference critical void ratio, and λ_c and ξ are two other material constants (for most sands $\xi = 0.7$) while p_{at} refers to the atmospheric pressure used for normalization.

The 'state parameter' $\psi = e - e_c$ can now be used as a measure of how far the material state e, p is from the critical state.

3.2. Elasticity

The isotropic hypoelasticity assumption is adopted in this model and is defined by

$$\dot{e}^e_{ij} = \frac{\dot{s}_{ij}}{2G}, \quad \dot{\epsilon}^e_v = -\frac{\dot{p}}{K} \tag{21}$$

The elastic shear modulus G is adopted from Richart et al. (1970). Assuming a constant Poisson's ratio ν, the elastic bulk modulus K can be found from the corresponding elastic shear modulus

$$G = G_0 \frac{(2.97 - e)^2}{(1 + e)} \left(\frac{p}{p_{at}}\right)^{1/2} p_{at} \quad ; \quad K = \frac{2(1+\nu)}{3(1-2\nu)} G \tag{22}$$

where G_0 is a material constant, e is the void ratio, and p_{at} is the atmospheric pressure used for normalization.

3.3. Yield Function

The yield function is defined by

$$f = [(s_{ij} - p\alpha_{ij})(s_{ij} - p\alpha_{ij})]^{1/2} - \sqrt{\frac{2}{3}} mp = 0 \tag{23}$$

where α_{ij} is the deviatoric back stress-ratio tensor, and m is a material constant. The above equation describes geometrically a 'cone' in the multiaxial stress space. The trace of the cone on the stress ratio π-plane is a circular deviatoric yield surface with center α_{ij} and radius $\sqrt{2/3}m$ as shown in Figure (1). The cone type yield surface implies that only changes of the stress ratio can cause plastic deformations. In a more recent version of this family of models, Taiebat and Dafalias (2008) have introduced a closed yield surface in the form of a modified eight-curve equation with proper hardening mechanism for capturing the plastic strain under constant stress to circumvent the mentioned limitation.

In order to incorporate the effect of the third invariant of the stress tensor in the model, an effective Lode angle θ is defined using 'unit' gradient tensor to the yield surface on the deviatoric plane, n_{ij}, as

$$\cos 3\theta = -\sqrt{6} n_{ij} n_{jk} n_{ki} \quad ; \quad n_{ij} = \frac{s_{ij} - p\alpha_{ij}}{[(s_{ij} - p\alpha_{ij})(s_{ij} - p\alpha_{ij})]^{1/2}} \tag{24}$$

and $0 \leq \theta \leq \pi/3$. This equation results in $\theta = 0$ for triaxial compression and $\theta_n = \pi/3$ for triaxial extension.

The critical stress ratio M at any effective Lode angle θ can be interpolated between M_c and M_e, i.e. the triaxial compression and extension critical stress ratios, respectively.

$$M = M_c g(\theta, c) \quad ; \quad g(\theta, c) = \frac{2c}{(1+c) - (1-c)\cos 3\theta} \quad ; \quad c = \frac{M_e}{M_c} \tag{25}$$

The model employs two ever–changing surfaces with the state parameter ψ, namely bounding and dilatancy surfaces, in order to account for the hardening/softening and dilatancy/contractancy response of sand. Upon shearing these two surfaces change (move) toward a fixed critical state surface to make the model fully compatible with critical state soil mechanics requirement. The line from the origin of the stress ratio π-plane parallel to n_{ij} will intersect the three concentric and homologous bounding, critical and dilatancy surfaces at the so-called 'image' back-stress ratio tensor α^b_{ij}, α^c_{ij}, and α^d_{ij} respectively as illustrated in

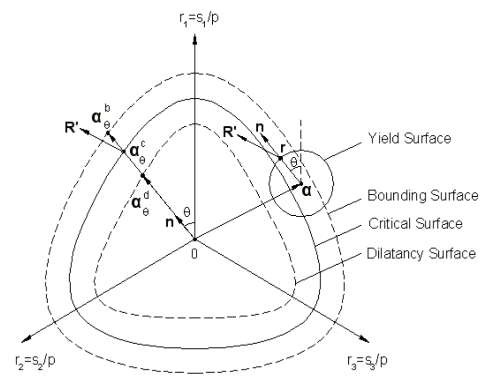

Figure 1. Schematic illustration of the yield, critical, dilatancy, and bounding surfaces in the π-plane of deviatoric stress ratio space (after Dafalias and Manzari (2004)).

Figure 1. The corresponding values of the aforementioned tensors are

$$\alpha^b_{ij} = \sqrt{\frac{2}{3}}[M\exp(-n^b\psi) - m]n_{ij} = \left(\sqrt{\frac{2}{3}}\alpha^b_\theta\right)n_{ij} \tag{26a}$$

$$\alpha^c_{ij} = \sqrt{\frac{2}{3}}[M - m]n_{ij} = \left(\sqrt{\frac{2}{3}}\alpha^c_\theta\right)n_{ij} \tag{26b}$$

$$\alpha^d_{ij} = \sqrt{\frac{2}{3}}[M\exp(n^d\psi) - m]n_{ij} = \left(\sqrt{\frac{2}{3}}\alpha^d_\theta\right)n_{ij} \tag{26c}$$

where $\psi = e - e_c$ is the state parameter and n^b and n^d are material constants.

3.4. Plastic Flow

In general the model employs a non-associative flow rule. The plastic strain is given by

$$\Delta\epsilon^p_{ij} = \Delta\lambda R_{ij} = \Delta\lambda(R'_{ij} - \frac{1}{3}D\delta_{ij}) \tag{27}$$

where $\Delta\lambda$ is the non-negative loading index. The deviatoric part R'_{ij} of the flow direction R_{ij}

is defined as the deviatoric part of the normal to the critical surface at the image point α^c_{ij}.

$$R'_{ij} = B n_{ij} + C(n_{ik} n_{kj} - \frac{1}{3}\delta_{ij}) \tag{28a}$$

$$B = 1 + \frac{3}{2}\frac{1-c}{c} g \cos 3\theta, \quad C = 3\sqrt{\frac{3}{2}}\frac{1-c}{c} g \tag{28b}$$

The dilatancy coefficient D in Equation (27) is defined by

$$D = A_d(\alpha^d_{ij} - \alpha_{ij}) n_{ij} = A_d \left(\sqrt{\frac{2}{3}} \alpha^d_\theta - \alpha_{ij} n_{ij} \right) \tag{29}$$

where parameter A_d is a function of the state variables. In order to account for the effect of fabric change during dilatancy, the so-called fabric-dilatancy internal variable z_{ij} has been introduced with an evolution law which will be presented later. The parameter A_d in Equation (29) now can be affected by the aforementioned tensor as

$$A_d = A_0(1 + \langle z_{ij} n_{ij} \rangle) \tag{30}$$

where A_0 is a material constant. The MacCauley brackets $\langle\rangle$ operate according to $\langle x \rangle = x$, if $x > 0$ and $\langle x \rangle = 0$, if $x \le 0$.

3.5. Evolution Laws

This model has two tensorial internal variables, namely, the back stress-ratio tensor α_{ij} and the fabric-dilatancy tensor z_{ij}. The evolution law for the back stress-ratio tensor α_{ij} is function of the distance between bounding and current back stress ratio tensor in the form of

$$\dot{\alpha}_{ij} = \dot{\lambda}[\frac{2}{3} h(\alpha^b_{ij} - \alpha_{ij})] \tag{31}$$

with h a positive function of state parameters. It is defined as a function of e, p, and η as follows in order to increase the efficiency of the model in handling the nonlinear response and reverse loading.

$$h = \frac{b_0}{(\alpha_{ij} - \tilde{\alpha}_{ij})n_{ij}} \tag{32a}$$

$$b_0 = G_0 h_0 (1 - c_h e) \left(\frac{p}{p_{at}}\right)^{-1/2} \tag{32b}$$

where $\tilde{\alpha}_{ij}$ is the initial value of α_{ij} at initiation of a new loading process and is updated to the new value when the denominator of Equation (32a) becomes negative. The h_0 and c_h are material constants. Finally the evolution law for the fabric-dilatancy tensor z_{ij} is introduced as

$$\dot{z}_{ij} = -c_z \left\langle -\dot{\lambda} D \right\rangle (z_{max} n_{ij} + z_{ij}) \tag{33}$$

with c_z and z_{max} as the material constants that control the maximum value of z_{ij} and its pace of evolution. Equations (30) and (33) are introduced to enhance the subsequent contraction in unloading after the dilation in loading to generate the well-known butterfly shape in the undrained cyclic stress path.

4. Verification and Validation Examples

Prediction of mechanical behavior comprises use of computational model to foretell the state of a physical system under consideration under conditions for which the computational model has not been validated (Oberkampf et al., 2002). Confidence in predictions relies heavily on proper Verification and Validation (V&V) process.

Verification is the process of determining that a model implementation accurately represents the developer's conceptual description and specification. It is a Mathematics issue. Verification provides evidence that the model is solved correctly. Verification is also meant to identify and remove errors in computer coding and verify numerical algorithms and is desirable in quantifying numerical errors in computed solution.

Validation is the process of determining the degree to which a model is accurate representation of the real world from the perspective of the intended uses of the model. It is a Physics issue. Validation provides evidence that the correct model is solved. Validation serves two goals, namely, (a) tactical goal in identification and minimization of uncertainties and errors in the computational model, and (b) strategic goal in increasing confidence in the quantitative predictive capability of the computational model.

Verification and Validation (V&V) procedures are the primary means of assessing accuracy in modeling and computational simulations. The V&V procedures are essential tools in building confidence and credibility in modeling and computational simulations. Figure (4) depicts relationships between verification, validation and the computational solution.

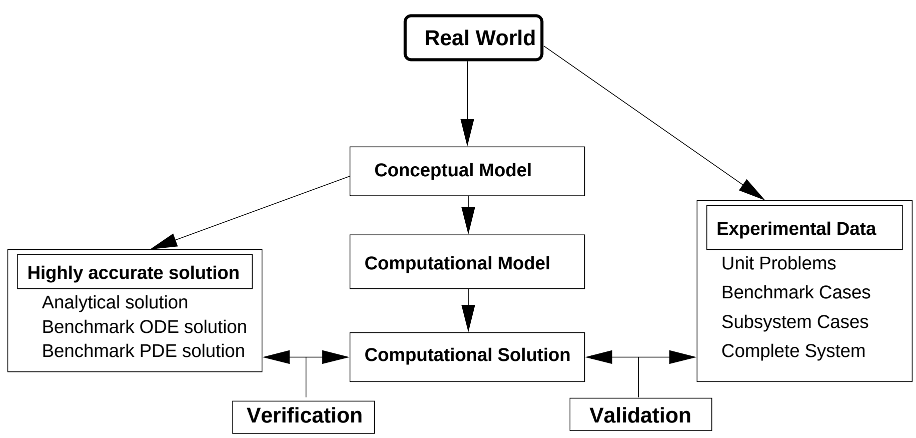

Figure 2. Schematic description of Verification and Validation procedures and the computational solution. (adopted from Oberkampf et al. (2002)).

In order to verify the u–p–U formulation, a number of closed form or very accurate solutions were used. Presented bellow are select examples used for verification. In particular, vertical (1D) consolidation, line injection of fluid in a reservoir and shock wave propagation in porous medium examples are used to verify the formulation and implementation. It should be noted that comparison of numerical and closed form solutions (verification) is satisfactory within the limitations of numerical accuracy whereby errors are introduced by finite element discretization, finite time step size and other artifacts of finite precision arithmetic. In addition to formulation verification, numerical implementation was verified using a comprehensive set of software tools available at the Computational Geomechanics Lab at UCD. Validation was performed on set of physical tests on Toyoura sand and is also presented below.

4.1. Verification: Vertical Consolidations

In this section, a vertical consolidation solution is used to verify the u-p-U finite element formulation. For the case of linear isotropic elastic soil, Terzaghi (1943) developed an analytic solution (based on infinite trigonometric series). This solution is used to verify low frequency solid-fluid coupling problem.

The consolidation model is assumed to have a depth of H_0, Young's modulus E, Poisson's ratio ν, permeability k, and the vertical load at the surface is p_0. Finite element model is represented with 10 brick elements with appropriate boundary conditions to mimic 1-D consolidation.

It is important to note that the analytic solutions for the vertical consolidation is based on assumption that both the soil particles and the pore fluid (water) are completely incompressible. Developed $u-p-U$ finite element model, can simulate realistic compressibility of soil particles and pore fluid. However, in this case, for the purpose of verification the bulk modulus of soil particles and pore fluid was input as a large number to mimic their respective incompressibility. The parameters used for this model are shown in Table (I).

Table I. Parameters for the 1D consolidation soil model.

parameter	symbol	value
gravity acceleration	g	$9.8\ m/s^2$
soil matrix Young's Modulus	E	$2.0 \times 10^7\ kN/m^2$
soil matrix Poisson's ratio	v	0.2
soil density	ρ_s	$2.0 \times 10^3\ kg/m^3$
water density	ρ_f	$1.0 \times 10^3\ kg/m^3$
permeability	k	$1.0 \times 10^{-7}\ m/s$
solid particle bulk modulus	K_s	$1.0 \times 10^{20}\ kN/m^2$
fluid bulk modulus	K_f	$2.2 \times 10^9\ kN/m^2$
porosity	n	0.4

As an example, a comparison between the numerical and closed-form solution (equation (8.171) from Coussy (1995)) for the excess pore pressure isochrones is shown in Figure (3). The agreement is excellent with the note that for initial stages of loading (when time is close to 0) some differences become evident. This is to be expected and is an artifact of the time integration of FEM model. This situation is easily resolved using shorter time steps in FEM modeling. However, as this increase in precision of time integration is needed only at the very beginning of the analysis, we opt to use large time steps in order to have efficient long term solutions (which does not require such short time steps).

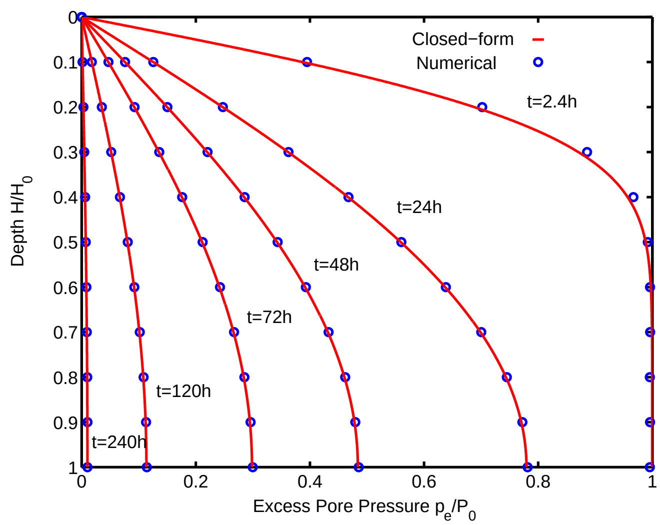

Figure 3. Numerical and closed-form excess pore pressure dissipation isochrones.

4.2. Verification: Line Injection of a fluid in a Reservoir

The analytical solution for the problem of line injection of fluid into a reservoir (porous medium) is also available from Coussy (1995). The problem is comprised of a reservoir of infinite extent composed of an isotropic, homogeneous and saturated poroelastic material. The cylindrical well of negligible dimensions, is used to inject a fluid in all directions orthogonal to the well axis (z). As a result of the axisymmetry, all quantities depends on distance r from the well only. The injection is assumed instantaneous at time $t = \Gamma$. The flow rate of fluid mass injection is constant and equal to q.

The finite element model used was made up of three dimensional brick elements. The axisymmetry was mimicked by creating 1/4 of the completely circular (axisymmetric) mesh. The use of 3D brick elements was done in order to verify their formulation and implementation, while one quarter of the mesh was used in order to facilitate application of boundary conditions, and since the problems is axisymmetric, to save on simulation requirements. In theory, any finite slice of the axisymmetric space cold have been chosen for the model, the alignment of radial boundaries with coordinate axes proves very useful in defining boundary conditions. Figure (4) shows the finite element model.

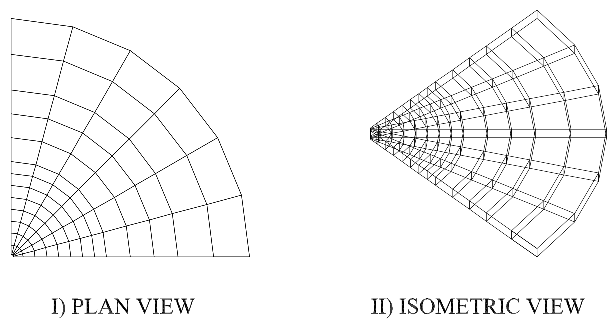

Figure 4. The mesh used for the study of line injection problem.

Table (II) presents material parameters and constants used in the analysis.

The results are recorded at three points at the radii of 10 cm, 50 cm and 85 cm. Comparison of analytic and numerical results are shown in Fig. (5). The comparison starts at 1 second after the injection. Comparison shows very good match between analytic and numerical solution. The (expected) mismatch is observed in the region close to the point of injection of fluid. In our case this point represents a singularity and for the finite element mesh, a very small opening was left in the mesh to mimic this (almost) singular point. As the distance from the singular injection point increases, the match between analytic and numerical solution becomes excellent. The match is also improving in time, that is, at 2 seconds, the match for both the pore pressures and the displacements is almost perfect, and it continues to improve as the time

Table II. Material Properties used to study the line injection problem

parameter	symbol	value
Poisson ratio	ν	0.2
Young's modulus	E	$1.2 \times 10^6\ kN/m^2$
Solid particle bulk modulus	K_s	$3.6 \times 10^7\ kN/m^2$
Fluid bulk modulus	K_f	$1.0 \times 10^{17}\ kN/m^2$
Solid density	ρ_s	$2700\ kg/m^3$
Fluid density	ρ_f	$1000\ kg/m^3$
Porosity	n	0.4
Permeability	k	$3.6 \times 10^{-6}\ m/s$

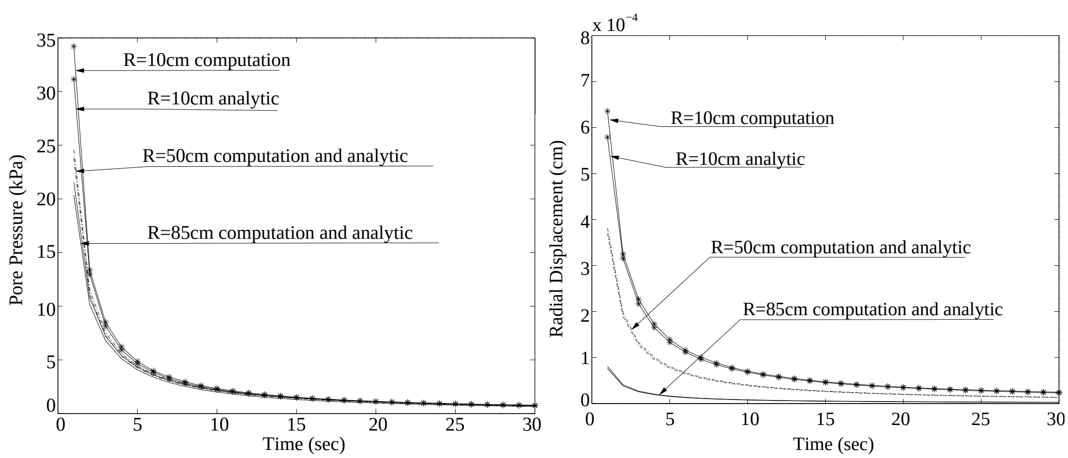

Figure 5. The comparison between analytical and computational solution for pore pressures (left) and radial displacements (right).

goes by.

4.3. Verification: Shock Wave Propagation in Saturated Porous Medium

In order to verify the dynamic behavior of the system, an analytic solution developed by Gajo Gajo (1995) and Gajo and Mongiovi Gajo and Mongiovi (1995) for 1D shock wave propagation in elastic porous medium was used. A model was developed consisting of 1000 eight node brick elements, with boundary conditions that mimic 1D behavior. In particular, no displacement of solid ($u_x = 0, u_y = 0$) and fluid ($U_x = 0, U_y = 0$) in x and y directions is allowed along the height of the model. Bottom nodes have full fixity for solid ($u_i = 0$) and fluid ($U_i = 0$) displacements while all the nodes above base are free to move in z direction for both solid and fluid. Pore fluid pressures are free to develop along the model. Loads to the model consist of a unit step function (Heaviside) applied as (compressive) displacements to both solid and fluid phases of the model, with an amplitude of 0.001 cm. The u–p–U model dynamic system of equations was integrated using Newmark algorithm (see section 2.4). Table III gives relevant parameters for this verification. Two set of permeability of material were used in our verification. The first model had permeability set $k = 10^{-6}$ cm/s which creates very high coupling between porous solid and pore fluid. The second model had permeability set to $k = 10^{-2}$ cm/s which, on the other hand creates a low coupling between porous solid and pore fluid. Comparison of simulations and the analytical solution are presented in Figure 6.

4.4. Validation: Material Model

Validation is performed by comparing experimental (physical) results and numerical (constitutive) simulations for the Toyoura sand. It should be noted that we have not done validation against 2D or 3D tests (say centrifuge tests) as characterization of sand used in

Table III. Simulation parameters used for the shock wave propagation verification problem.

Parameter	Symbol	Value
Poisson ratio	ν	0.3
Young's modulus	E	$1.2 \times 10^6\ kN/m^2$
Solid particle bulk modulus	K_s	$3.6 \times 10^7\ kN/m^2$
Fluid bulk modulus	K_f	$2.17 \times 10^6\ kN/m^2$
Solid density	ρ_s	$2700\ kg/m^3$
Fluid density	ρ_f	$1000\ kg/m^3$
Porosity	n	0.4
Newmark parameter	γ	0.6

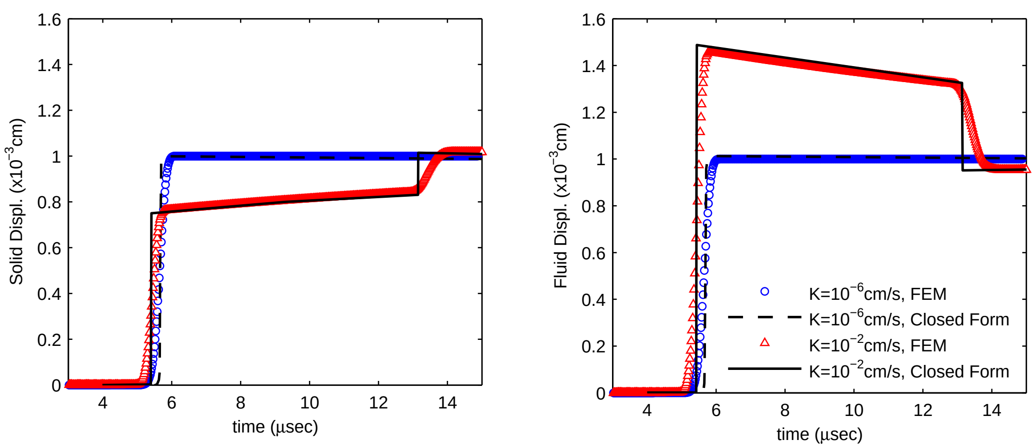

Figure 6. Compressional wave in both solid and fluid, comparison with closed form solution.

centrifuge experiments is usually less than complete for use with advanced constitutive models. Moreover, as our approach seeks to make predictions of prototype behavior, scaling down models (and using them for comparison with numerical predictions) brings forward issues of physics of scaling which we would rather stay out of. The material parameters used are from Dafalias and Manzari (2004) and are listed in Table (IV). Several simulated results are compared with the experimental data published by Verdugo and Ishihara (1996).

Table IV. Material parameters of Dafalias-Manzari model.

material parameter		value	material parameter		value
Elasticity	G_0	125 kPa	Plastic modulus	h_0	7.05
	v	0.05		c_h	0.968
Critical sate	M	1.25		n_b	1.1
	c	0.712	Dilatancy	A_0	0.704
	λ_c	0.019		n_d	3.5
	ξ	0.7	Fabric-dilatancy	z_{max}	4.0
	e_r	0.934		c_z	600.0
Yield surface	m	0.01			

Figure (7) presents both loading and unloading triaxial drained test simulation results for a relatively low triaxial isotropic pressure of 100 kPa but with different void ratios of $e_0 = 0.831, 0.917, 0.996$ at the end of isotropic compression. During the loading stage, one can observes the hardening and then softening together with the contraction and then dilation for the denser sand, while only hardening together with contraction for the looser sand. The significance of the state parameter to the soil modeling is clear from the very different responses

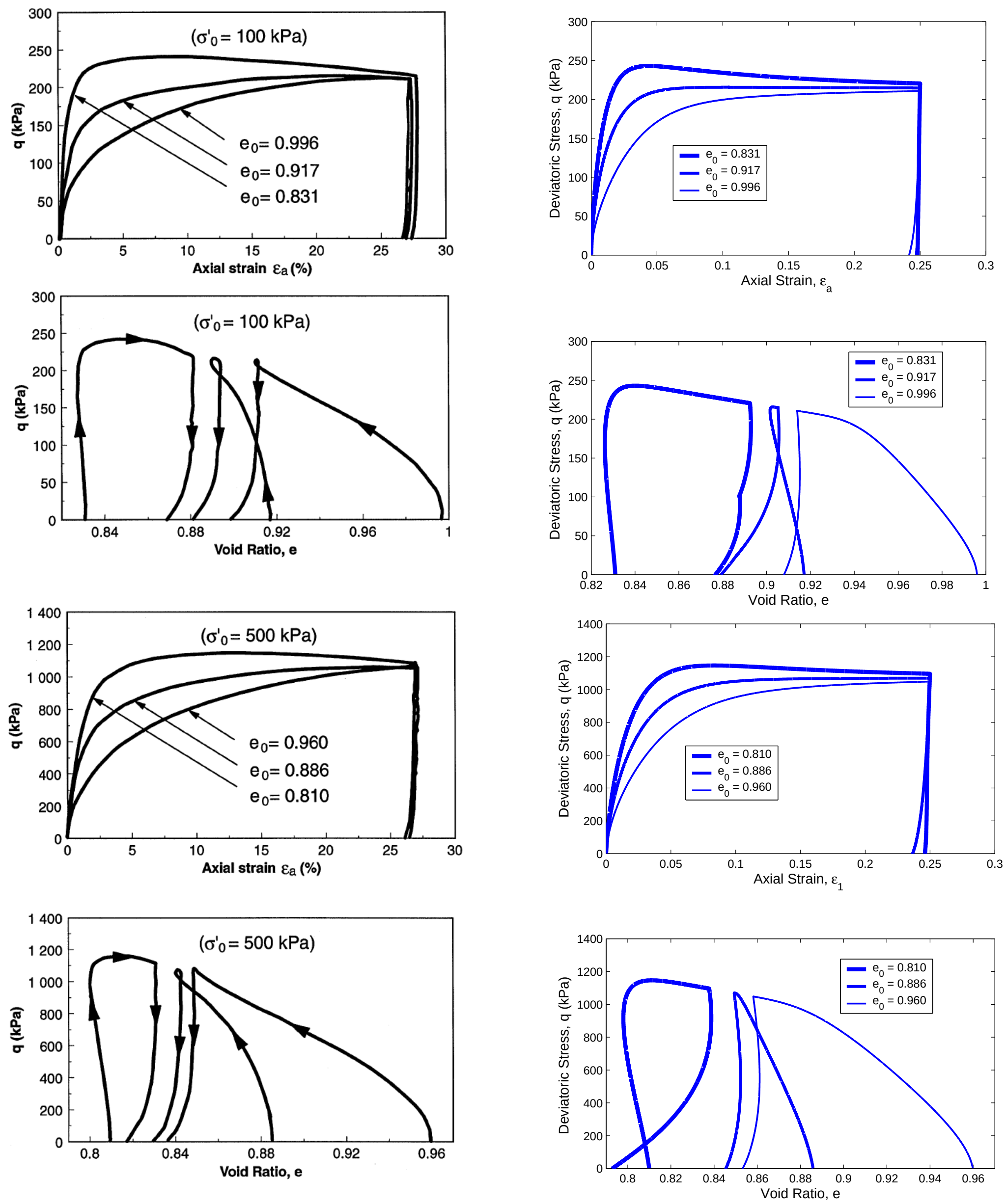

Figure 7. Left: Experimental data; Right: Simulated results.

with different void ratios at the same triaxial isotropic pressure.

Figure (7) also shows both loading and unloading triaxial drained test simulation results for a relatively high triaxial isotropic pressure of 500 kPa but with different void ratio of e_0=0.810, 0.886, 0.960 at the end of isotropic compression. Similar phenomenon are observed as with tests (physical and numerical) for relatively low triaxial isotropic pressure. However, due to the higher confinement pressure, the stress-strain responses are higher at the same strain, which proves the significant pressure dependent feature for the sands.

Figure (8) presents both loading and unloading triaxial undrained test simulation results for a dense sand with the void ratio of e_0=0.735 at the end of isotropic compression but with different isotropic compression pressures of p_0 = 100, 1000, 2000, 3000 kPa. During the loading stage, one observes that each of responses are close to the critical state line for the very various range of isotropic compression pressures. For the higher isotropic compression pressure, the contraction response with softening is clearly observed, while for the smaller isotropic compression pressure, it is a dilation response without softening.

Close matching of physical testing data with constitutive predictions represents a satisfactory validation of our material model. This validation with previous verification gives us confidence that predictions (presented in next section) represent well the real, prototype behavior.

5. Liquefaction of Level and Sloping Grounds

Liquefaction of level and sloping grounds represents a very common behavior during earthquakes. Of interest is to estimate settlement for level ground, and horizontal movements for sloping grounds. In next few sections, presented are results for a 1D, vertical (level ground) and sloping ground cases for dense and loose sand behavior during seismic shaking.

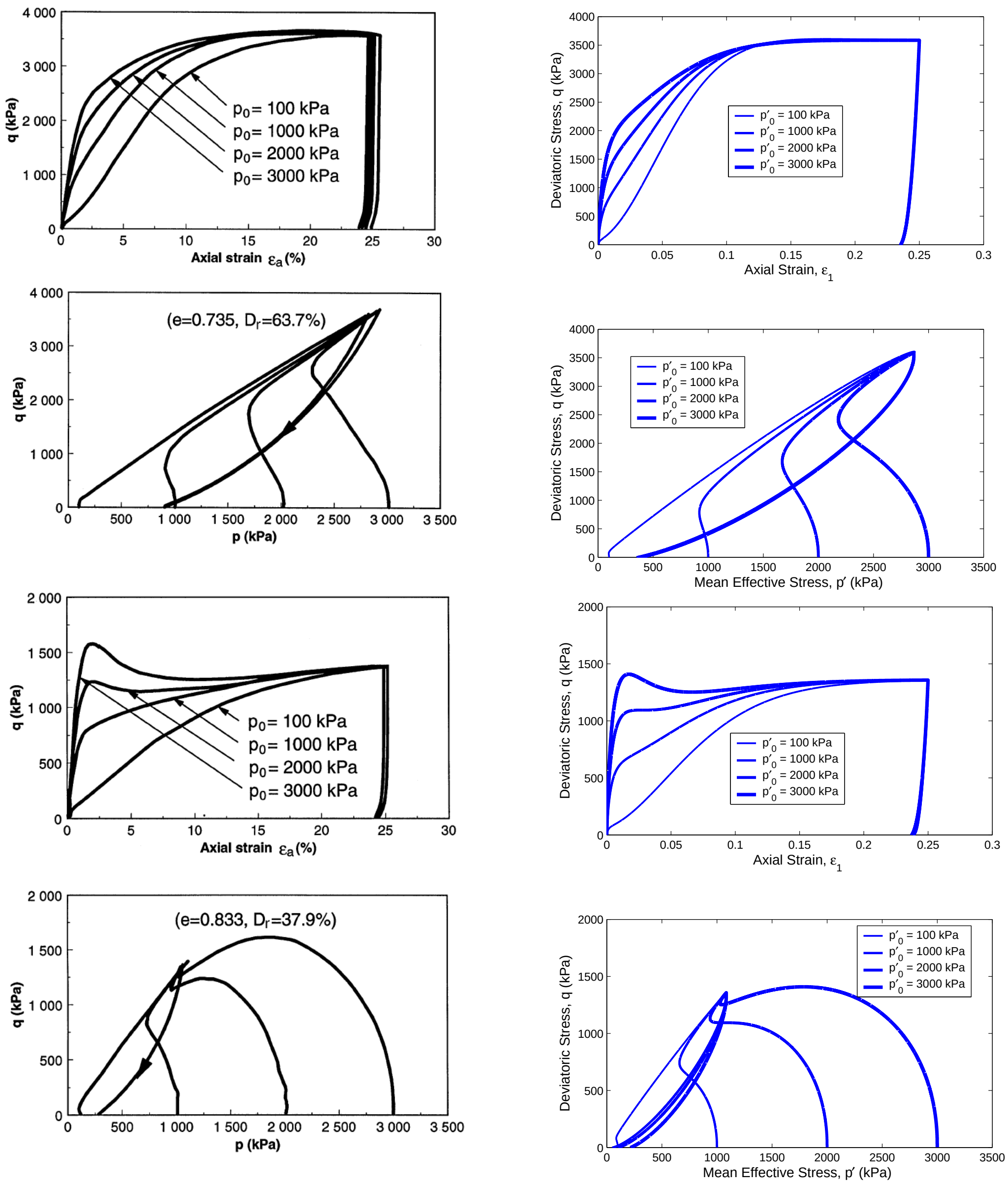

Figure 8. Left: Experimental data; Right: Simulated results.

Table V. Additional parameters used in boundary value problem simulations (other than material parameters from the Table (IV)).

Parameter	Symbol	Value
Solid density	ρ_s	2700 kg/m^3
Fluid density	ρ_f	1000 kg/m^3
Solid particle bulk modulus	K_s	3.6×10^7 kN/m^2
Fluid bulk modulus	K_f	2.2×10^6 kN/m^2
permeability	k	5.0×10^{-4} m/s
HHT parameter	α	-0.2

5.1. Model Description

Vertical soil column consists of a multiple-elements subjected to an earthquake shaking. The soil is assumed to be Toyoura sand and the calibrated parameters are from Dafalias and Manzari (2004), and were given in the Table (IV). The other parameters, related to the boundary value problem are given in table (V).

For tracking convenience, the mesh elements are labeled from E01 (bottom) to E10 (surface) and nodes at each layers are labeled from A (bottom) to K (surface).

A static application of gravity analysis is performed before seismic excitation. The resulting fluid hydrostatic pressures and soil stress states along the soil column serve as initial conditions for the subsequent dynamic analysis.

It should be noted that the self weight loading is performed on an initially zero stress (unloaded) soil column and that the material model and numerical integration algorithms are powerful enough to follow through this early loading with proper evolution. The boundary conditions are such that the soil and water displacement degree of freedom (DOF) at the bottom surface are fixed, while the pore pressure DOFs are free; the soil and water displacement DOFs at the upper surface are free upwards to simulate the upward drainage. The pore pressure DOFs are fixed at surface thus setting pore pressure to zero. On the sides, soil skeleton and water are prevented from moving in horizontal directions while vertical movement of both is free. It is emphasized that those displacements (of soil skeleton and pore fluid) are different. In order to simulate the 1D behavior, all DOFs at the same depth level are connected in a master–slave fashion. Modeling of sloping ground is done by creating a constant horizontal load, sine of inclination angle, multiplied by the self weight of soil column, to mimic sloping ground. In addition to that, for a sloping ground, there should be a constant flow (slow) downhill, however this is neglected in our modeling. The permeability is assumed to be isotropic $k = 5.0\times10^{-4}$ m/s. The input acceleration time history (Figure (9)) is taken from the recorded horizontal acceleration of Model No.1 of VELACS project Arulanandan and Scott (1993) by Rensselaer Polytechnic Institute (http://geoinfo.usc.edu/gees/velacs/). The magnitude of the motion is close to 0.2 g, while main shaking lasts for about 12 seconds (from 1 s to 13 s). For the sloping ground model a slope of % 3 was considered.

It should be emphasized that the soil parameters are related to Toyoura sand, not Nevada sand which is used in VELACS project. The purpose of presented simulation is to show the predictive performance using verified and validated formulation, algorithms, implementation and models.

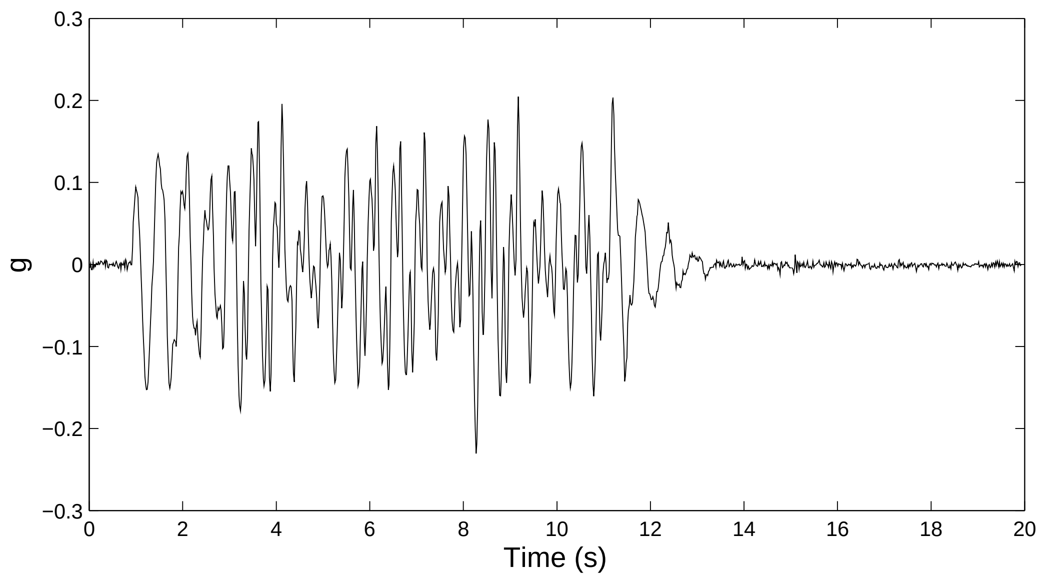

Figure 9. Input earthquake ground motion for the soil column.

5.2. Behavior of Saturated Level Ground

Figure (10) describes the response of the sample with loose sand $e_0 = 0.85$. This figure shows the typical mechanism of cyclic decrease in effective vertical stress due to pore pressure build up as expected for the looser than critical granular material. The lower layers show only the reduction of effective vertical stress from the beginning. Once the effective vertical (and therefore confining) stress approaches the smaller values, signs of the so-called butterfly shape can be observes in the stress path. Similar observation can made in the upper layers which have the smaller confining pressure comparing to the lower layers from the very beginning due to lower surcharge. The upper layers have lower confining pressure (lower surcharge) at the beginning of the shaking, hence less contractive response is expected in these layer; however, soon after the initiation of the shaking these top layers start showing the liquefaction state and that type of response continues even after the end of the shaking. The top section of the model has remained liquefied well past the end of shaking. This is explained by the large supply of pore fluid from lower layers, for which the dissipation starts earlier. For example, for the lowest layer, the observable drop in excess pore pressure start as soon as the shaking ends, while, the upper layers then receive this dissipated pore fluid from lower layers and do liquefy (or continue being liquefied) well past end of shaking (which happens at approximately 13 seconds). It is very important to note the significance of this incoming pore water flux on the pore water pressure of the top layers. Despite the less contractive response of soil skeleton at the top elements, the transient pore water flux, that enters these elements from the bottom, forces those to a liquefaction state. In other words, the top elements have not liquefied only due to their loose state but also because of the water flow coming from the bottom layers. The maximum horizontal strains can be observed in the middle layers due to liquefaction and prevents upper layers from experiencing larger strains. The displacements of water and soil are presented in the last column. It shows that in all layers the upward displacement of water is larger than the downward displacement of soil. This behavior reflects soil densification during shaking.

Figure (11) describes the response of the sample with dense sand ($e_0 = 0.75$). This figure also shows the typical mechanism of cyclic decrease in effective vertical stress. However, in case of this dense sample the decreasing rate of the effective confining pressure is much smaller than what was observed in the loose sample. Signs of the partial butterfly shape in the effective stress path can be observed from early stages of shaking. The butterfly is more evident in the upper layers with the lower confining pressure, i.e. more dilative response. In later stages of the shaking, i.e. when the confining pressure reduces to smaller value the butterfly shape of the stress path gets more pronounced due to having more dilative response in the lower confining pressure based on CSSM concept. In comparing this dense case to the case of shaking the loose sand column, the current case does not show any major sign of liquefaction (when stress ratio $r_u = 1$). This is due to the less contractive (more dilative) response of the sand in this case, which is coming from the the denser state of the sample. Because of having partial segments of dilative response, the whole column of the sand has not loosed its strength to the extent that happened for the case of loose sand and therefore smaller values of horizontal strains has been observed in the results. The absolute values of soil and water vertical displacements are also smaller than the case of loose sand which can be again referred to the less overall contractive response in this case.

Overall, it can be noted that the response in the case of loose sand ($e_0 = 0.85$) is mainly below the dilatancy surface (phase transformation surface) while the denser sand sample with $e_0 = 0.75$ shows partially dilative response referring to the denser than critical state.

5.3. Behavior of Saturated Sloping Ground

Figures (12) and (13) present the result of the numerical simulations for shaking the inclined soil columns (toward right) with loose and dense sand samples, respectively. The inclination of the soil column results in presence of the offset shear stress to the right side. This essentially poses asymmetric horizontal shear stresses (toward the direction of inclination) during cycles of shaking. On one hand, this offset shear stress makes the sample more dilative in the parts of shaking toward the right side (think about the state distance from the phase transformation line or dilatancy line in the $p - q$ space). As a result asymmetric butterfly loops will be induced causing the soil to regain its stiffness and strength (p) in the dilative parts of the

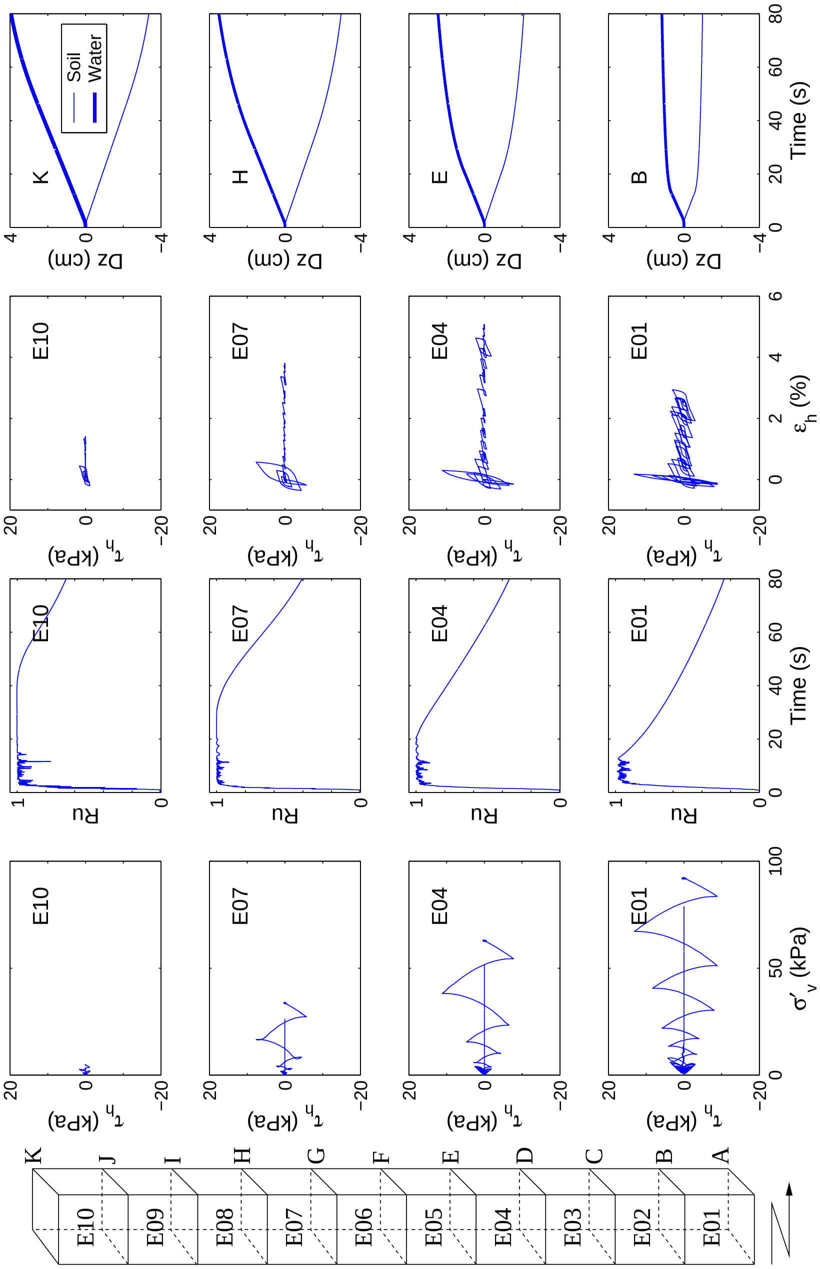

Figure 10. Seismic results for (loose sand) soil column in level ground ($e_0 = 0.85$).

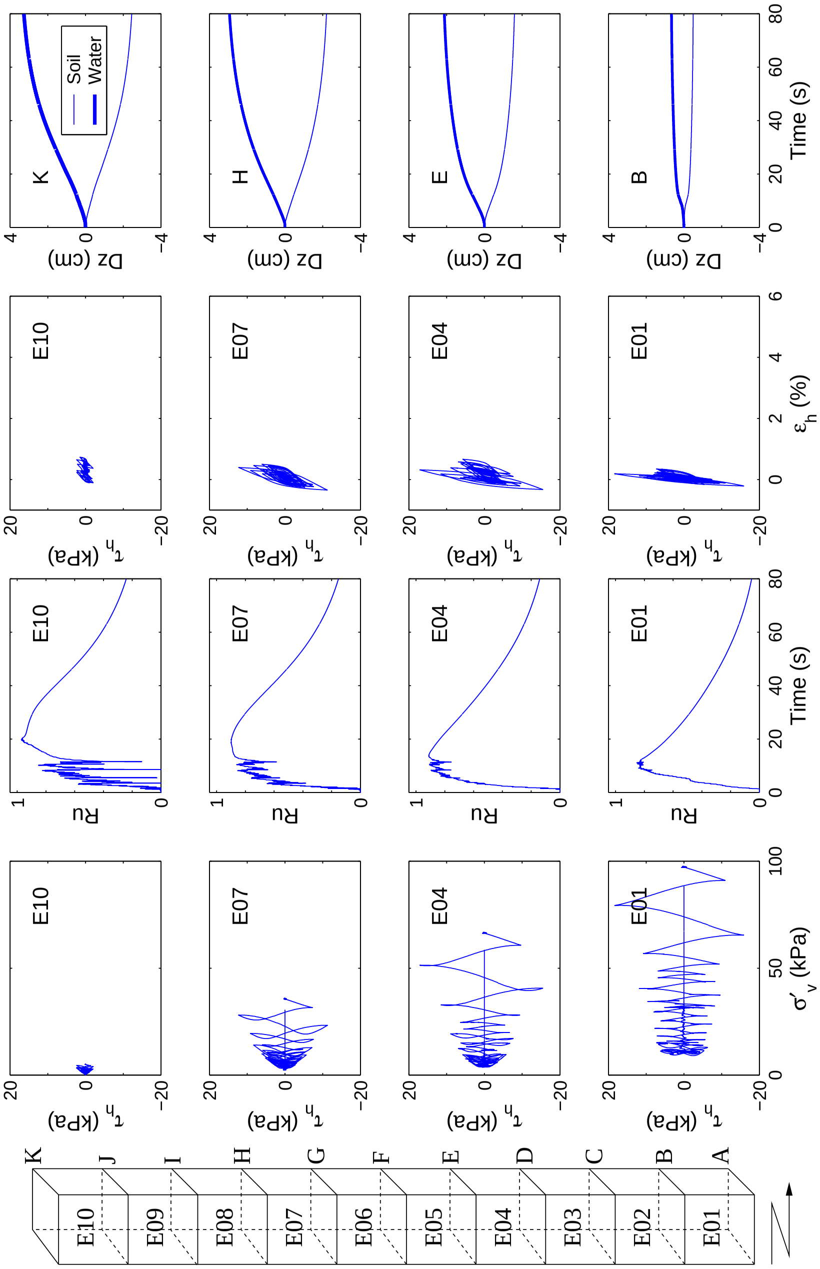

Figure 11. Seismic results for (dense sand) soil column in level ground ($e_0 = 0.75$).

corresponding cycles, therefore only instantaneous spikes of $r_u = 1$ can be observed in case of the sloped columns of soil. There is also a permanent liquefaction in terms of having stationary portions of $r_u = 1$ in this case. On the other hand, the offset shear stress results generation of more horizontal strains in the portions of loading which are directed toward the right side than those which are directed back toward the left side. As a result the horizontal shear strains will accumulative toward the right side and create larger permanent horizontal displacement comparing to the case of level ground soil column. Since the overall dilative response of the dense sample, i.e. Figure (13), is larger than that of the loose sample, i.e. Figure (12), the dense sample shows stiffer response and therefore less accumulative horizontal shear strains than the loose sample. The difference in predicted horizontal displacements is almost three times, that is, for the dense sample the final, maximum horizontal displacement is approx. 0.5 m, while for the loose sand sample, it almost 1.5 m,

6. Summary

A numerical modeling approach was presented accounting for fully coupled (elastic–plastic porous solid – fluid) behavior of soils using $u - p - U$ formulation. A critical state elasto–plastic model accounting for the fabric dilatancy effects was used for all stages of loading, starting from zero stress state, through self weight and finally to seismic shaking. The formulation and implementation takes into account velocity proportional damping (usually called viscous damping) by proper modeling of coupling of pore fluid and solid skeleton, while the displacement proportional damping is appropriately modeled using elasto–plasticity and a powerful material model. No additional damping was used in FEM model. The formulation and resulting implementation were verified and validate using a number of unit tests and were

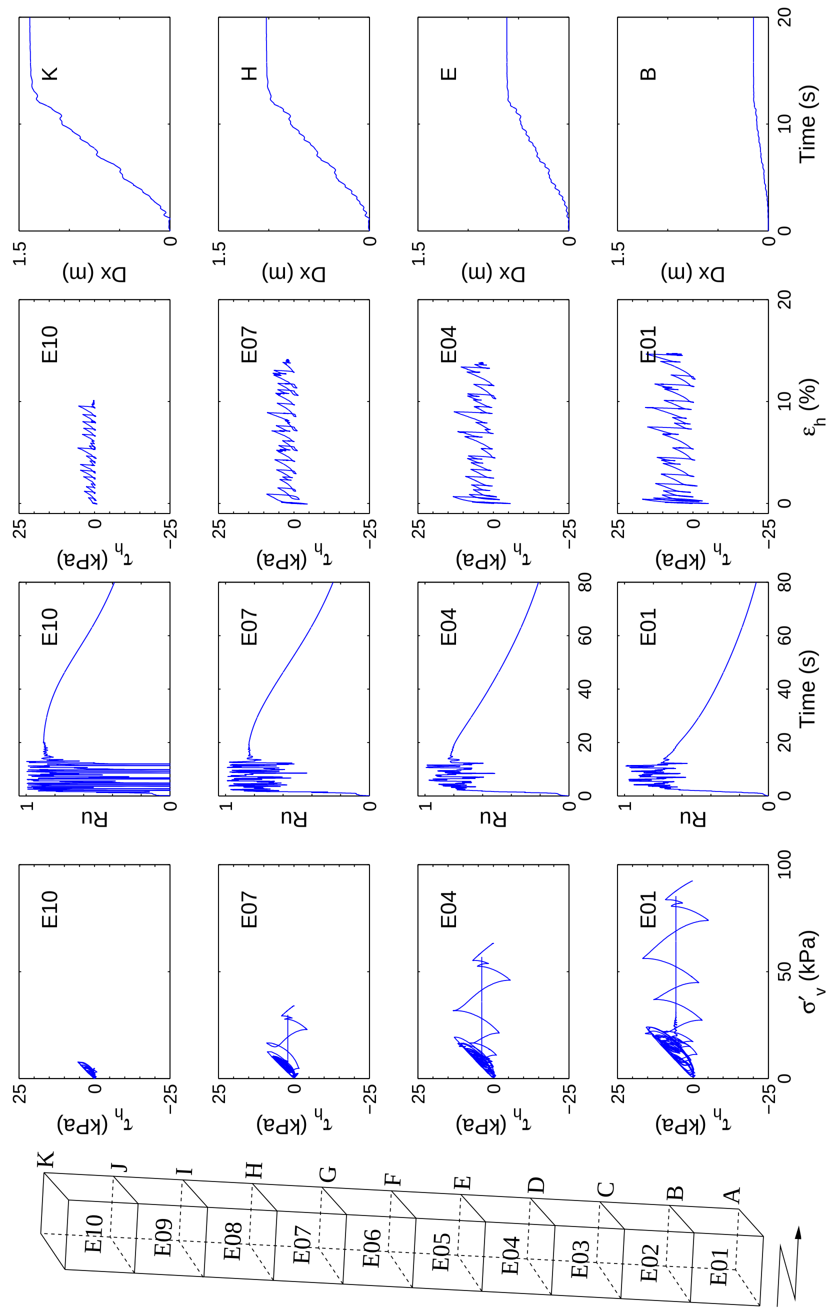

Figure 12. Seismic results for (loose sand) soil column in sloping ground ($e_0 = 0.85$).

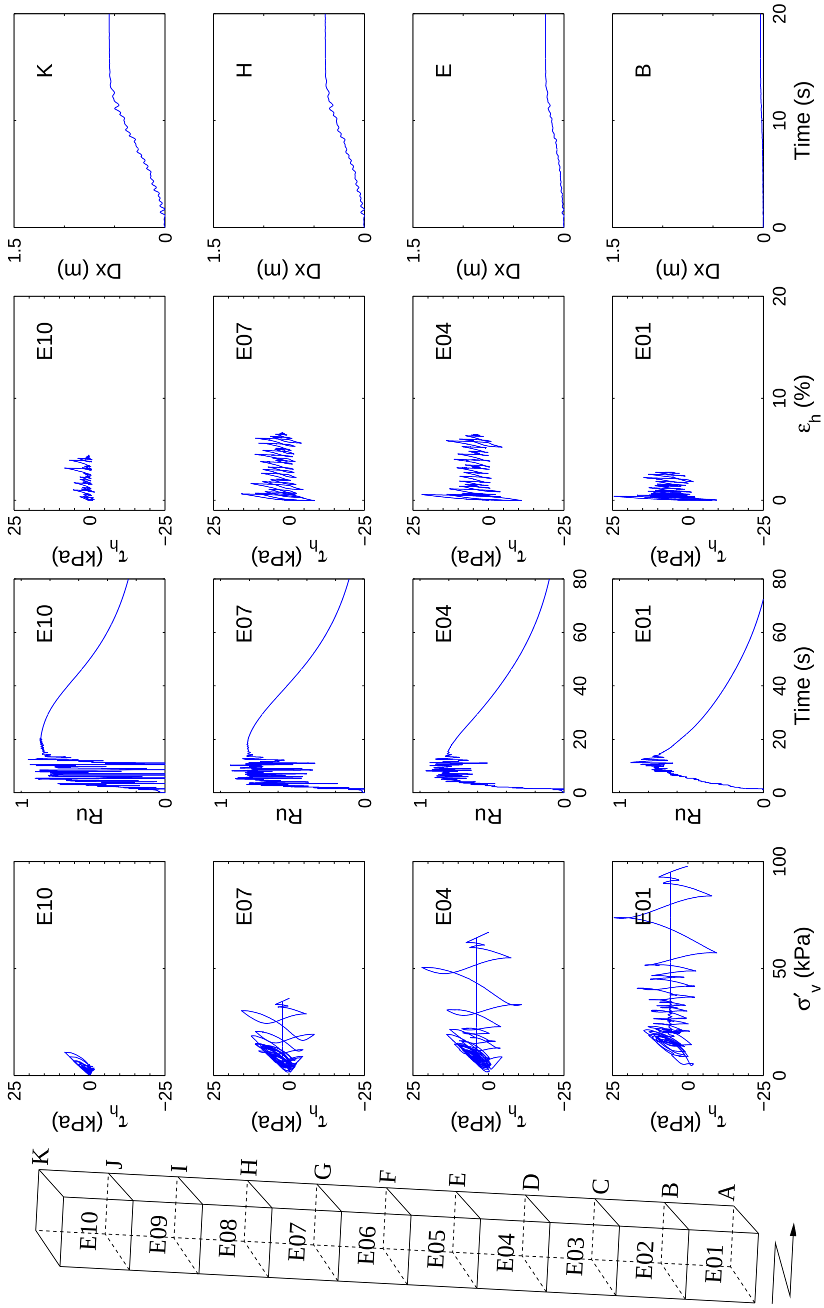

Figure 13. Seismic results for (dense sand) soil column in sloping ground ($e_0 = 0.75$).

then applied to the problem of sand liquefaction and cyclic mobility phenomena.

Presented verified formulation and implementation, in conjunction with a validated material model give us confidence in our ability to realistically predict behavior of saturated soils during dynamic loading events. Moreover, the developed system, that is closely following the physics (mechanics) of the problem, allows for investigation of energy dissipation mechanisms during seismic events. As such it allows for high fidelity simulations that will allow designers to make a transition from empirically based to rational mechanics based methods.

references

John Argyris and Hans-Peter Mlejnek. Dynamics of Structures. North Holland in USA Elsevier, 1991.

Kandiah Arulanandan and Ronald F. Scott, editors. Verification of Numerical Procedures for the Analysis of Soil Liquefaction Problems. A. A. Balkema, 1993.

Andrew Hin-Cheong Chan. A Unified Finite Element Solution to Static and Dynamic Problems in Geomecahnics. PhD thesis, Department of Civil Engineering, University College of Swansea, February 1988.

Olivier Coussy. Mechanics of Porous Continua. John Wiley and Sons, 1995. ISBN 471 95267 2.

Yannis F. Dafalias and Majid T. Manzari. Simple plasticity sand model accounting for fabric change effects. Journal of Engineering Mechanics, 130(6):622–634, 2004.

Timothy A. Davis and Iain S. Duff. A combined unifrontal/multifrontal method for unsymmetric sparse matrices. Technical Report TR97-016 (UofF) and TR-97-046 (RAL), University of Florida and Rutherford Appleton Laboratory, 1997.

J. E. Dennis, Jr. and Robert B. Schnabel. Numerical Methods for Unconstrained Optimization and Nonlinear Equations. Prentice Hall , Engelwood Cliffs, New Jersey 07632., 1983.

Ahmed Elgamal, Zhaohui Yang, and Ender Parra. Computational modeling of cyclic mobility and post–liquefaction site response. Soil Dynamics and Earthquake Engineering, 22:259–271, 2002.

Ahmed Elgamal, Zhaohui Yang, Ender Parra, and Ahmed Ragheb. Modeling of cyclic mobility in saturated cohesionless soils. International Journal of Plasticity, 19(6):883–905, 2003.

A. Gajo. Influence of viscous coupling in propagation of elastic waves in saturated soil. ASCE Journal of Geotechnical Engineering, 121(9):636–644, September 1995.

A. Gajo and L. Mongiovi. An analytical solution for the transient response of saturated linear elastic porous media. International Journal for Numerical and Analytical Methods in Geomechanics, 19(6):399–413, 1995.

A. Gajo, A. Saetta, and R. Vitaliani. Evaluation of three– and two–field finite element methods for the dynamic response of saturated soil. International Journal for Numerical Methods in Engineering, 37:1231–1247, 1994.

H. M. Hilber, T. J. R. Hughes, and R. L. Taylor. Improved numerical dissipation for time integration algorithms in structural dynamics. Earthquake Engineering and Structural Dynamics, 5:283–292, 1977.

T. J. R. Hughes and W. K. Liu. Implicit–explicit finite elements in transient analysis: Stability theory. ASME Journal of Applied Mechanics, 45:371–374, June 1978a.

T. J. R. Hughes and W. K. Liu. Implicit–explicit finite elements in transient analysis: Implementation and numerical examples. ASME Journal of Applied Mechanics, 45:375–378, June 1978b.

Thomas J. R. Hughes. The Finite Element Method ; Linear Static and Dynamic Finite Element Analysis. Prentice Hall Inc., 1987.

Boris Jeremić. Line search techniques in elastic–plastic finite element computations in geomechanics. Communications in Numerical Methods in Engineering, 17(2):115–125, January 2001.

Boris Jeremić and Stein Sture. Implicit integrations in elasto–plastic geotechnics. International Journal of Mechanics of Cohesive–Frictional Materials, 2:165–183, 1997.

Boris Jeremić and Stein Sture. Tensor data objects in finite element programming. International Journal for Numerical Methods in Engineering, 41:113–126, 1998.

Boris Jeremić and Zhaohui Yang. Template elastic–plastic computations in geomechanics. International Journal for Numerical and Analytical Methods in Geomechanics, 26(14):1407–1427, 2002.

X. S. Li and Y. Wang. Linear representation of steady-state line for sand. Journal of Geotechnical and Geoenvironmental Engineering, 124(12):1215–1217, 1998.

M. T. Manzari and Y. F. Dafalias. A critical state two–surface plasticity model for sands. Géotechnique, 47(2):255–272, 1997.

Francis Thomas McKenna. Object Oriented Finite Element Programming: Framework for Analysis, Algorithms and Parallel Computing. PhD thesis, University of California, Berkeley, 1997.

N. M. Newmark. A method of computation for structural dynamics. ASCE Journal pf the Engineering Mechanics Division, 85(67-94), 1959.

William L. Oberkampf, Timothy G. Trucano, and Charles Hirsch. Verification, validation and predictive capability in computational engineering and physics. In Proceedings of the Foundations for Verification and Validation on the 21st Century Workshop, pages 1–74, Laurel, Maryland, October 22-23 2002. Johns Hopkins University / Applied Physics Laboratory.

M. Pastor, O. C. Zienkiewicz, and A. H. C. Chan. Generalized plasticity and the modeling of soil behaviour. International Journal for Numerical and Analytical Methods in Geomechanics, 14:151–190, 1990.

Jean H. Prevost. Wave propagation in fluid-saturated porous media: an efficient finite element procedure. Soil Dynamics and Earthquake Engineering, 4(4):183 –202, 1985.

F. E. Richart, J. R. Hall, and R. D. Woods. Vibration of Soils and Foundations, International Series in Theoretical and Applied Mechanics. Prentice-Hall, Englewood Cliffs, N.J., 1970.

Patrick J. Roache. Verification and Validation in Computational Science and Engineering. Hermosa Publishers, Albuquerque, New Mexico, 1998. ISBN 0-913478-08-3.

B. R. Simon, J. S.–S. Wu, O. C. Zienkiewicz, and D. K. Paul. Evaluation of $u - w$ and $u - \pi$ finite element methods for the dynamic response of saturated porous media using one–dimensional models. International Journal for Numerical and analytical methods in Geomechanics, 10:461–482, 1984a.

B. R. Simon, O. C. Zienkiewicz, and D. K. Paul. An analytical solution for the transient response of saturated porous elastic solids. International Journal for Numerical and analytical methods in Geomechanics, 8:381–398, 1984b.

Ranbir S.Sandhu, H.L. Shaw, and S.J. Hong. A three-field finite element procedure for analysis of elastic wave propagation through fluid-saturated soils. Soil Dynamics and Earthquake Engineering, 9:58–65, 1990.

Mahdi Taiebat and Yannis F. Dafalias. SANISAND: Simple anisotropic sand plasticity model. International Journal for Numerical and Analytical Methods in Geomechanics, 2008. (in print, available in earlyview).

Mahdi Taiebat, Hadi Shahir, and Ali Pak. Study of pore pressure variation during liquefaction using two constitutive models for sand. Soil Dynamics and Earthquake Engineering, 27: 60–72, 2007.

Karl Terzaghi. Theoretical Soil Mechanics. Wiley, New York, 1943.

Ramon Verdugo and Kenji Ishihara. The steady state of sandy soils. Soils and Foundations, 36(2):81–91, 1996.

O. C. Zienkiewicz and T. Shiomi. Dynamic behaviour of saturated porous media; the generalized Biot formulation and its numerical solution. International Journal for Numerical Methods in Engineering, 8:71–96, 1984.

O. C. Zienkiewicz and R. L. Taylor. The Finite Element Method, Volume 1, The Basis, 5th Edition. Butterworth Heinemann, London, 2000.

O. C. Zienkiewicz, A. H. C. Chan, M. Pastor, B. A. Schrefler, and T. Shiomi. Computational Geomechanics with Special Reference to Earthquake Engineering. John Wiley and Sons., 1999. ISBN 0-471-98285-7.

O.C. Zienkiewicz, C. T. Chang, and P. Bettess. Drained, undrained, consolidating and dynamic behaviour assumptions in soils. Géotechnique, 30(4):385–395, 1980.

Olgierd Cecil Zienkiewicz and Robert L. Taylor. The Finite Element Method, volume 1. McGraw - Hill Book Company, fourth edition, 1991a.

Olgierd Cecil Zienkiewicz and Robert L. Taylor. The Finite Element Method, volume 2. McGraw - Hill Book Company, Fourth edition, 1991b.